An FRB sent me a DM: constraining the electron column of the milky way halo with fast radio burst dispersion measures from CHIME/FRB

Cook, Amanda M.; Bhardwaj, Mohit; Gaensler, B. M.; Scholz, Paul; Eadie, Gwendolyn M.; Hill, Alex S.; Kaspi, Victoria M.; Masui, Kiyoshi W.; Curtin, Alice P.; Dong, Fengqiu Adam; Fonseca, Emmanuel; Herrera-Martin, Antonio; Kaczmarek, Jane; Lanman, Adam E.; Lazda, Mattias; Leung, Calvin; Meyers, Bradley W.; Michilli, Daniele; Pandhi, Ayush; Pearlman, Aaron B.; Pleunis, Ziggy; Ransom, Scott; Rahman, Mubdi; Sand, Ketan R.; Shin, Kaitlyn; Smith, Kendrick; Stairs, Ingrid; Stenning, David C.

Publisher's version / Version de l'éditeur:
https://doi.org/10.3847/1538-4357/acbbd0
The Astrophysical Journal, 946, 2, p. 58, 2023-03-30

The Astrophysical Journal, 946:58 (14pp), 2023 April 1 https://doi.org/10.3847/1538-4357/acbbd0

An FRB Sent Me a DM: Constraining the Electron Column of the Milky Way Halo with Fast Radio Burst Dispersion Measures from CHIME/FRB

Amanda M. Cook[1,2], Mohit Bhardwaj[3,4,5], B. M. Gaensler[1,2], Paul Scholz[2], Gwendolyn M. Eadie[1,6], Alex S. Hill[7,8], Victoria M. Kaspi[3,4], Kiyoshi W. Masui[9,10], Alice P. Curtin[3,4], Fengqiu Adam Dong[8], Emmanuel Fonseca[11,12], Antonio Herrera-Martin[1,6], Jane Kaczmarek[7], Adam E. Lanman[3,4], Mattias Lazda[4], Calvin Leung[9,10], Bradley W. Meyers[8,13], Daniele Michilli[9,10], Ayush Pandhi[1,2], Aaron B. Pearlman[3,4], Ziggy Pleunis[2], Scott Ransom[14], Mubdi Rahman[15], Ketan R. Sand[3,4], Kaitlyn Shin[9,10], Kendrick Smith[16], Ingrid Stairs[8], and David C. Stenning[17]

[1] David A. Dunlap Institute Department of Astronomy & Astrophysics, University of Toronto, 50 St. George Street, Toronto, ON M5S 3H4, Canada; cook@astro.utoronto.ca
[2] Dunlap Institute for Astronomy & Astrophysics, University of Toronto, 50 St. George Street, Toronto, ON M5S 3H4, Canada
[3] McGill Space Institute, McGill University, 3550 rue University, Montréal, QC H3A 2A7, Canada
[4] Department of Physics, McGill University, 3600 rue University, Montréal, QC H3A 2T8, Canada
[5] Department of Physics, Carnegie Mellon University, 5000 Forbes Avenue, Pittsburgh, PA 15213, USA
[6] Department of Statistical Science, University of Toronto, Ontario Power Building, 700 University Avenue, 9th Floor, Toronto, ON M5G 1Z5, Canada
[7] Dominion Radio Astrophysical Observatory, Herzberg Research Centre for Astronomy and Astrophysics, National Research Council Canada, P.O. Box 248, Penticton, BC V2A 6J9, Canada
[8] Department of Physics and Astronomy, University of British Columbia, 6224 Agricultural Road, Vancouver, BC V6T 1Z1 Canada
[9] MIT Kavli Institute for Astrophysics and Space Research, Massachusetts Institute of Technology, 77 Massachusetts Avenue, Cambridge, MA 02139, USA
[10] Department of Physics, Massachusetts Institute of Technology, 77 Massachusetts Avenue, Cambridge, MA 02139, USA
[11] Department of Physics and Astronomy, West Virginia University, P.O. Box 6315, Morgantown, WV 26506, USA
[12] Center for Gravitational Waves and Cosmology, West Virginia University, Chestnut Ridge Research Building, Morgantown, WV 26505, USA
[13] International Centre for Radio Astronomy Research (ICRAR), Curtin University, Bentley, WA 6102, Australia
[14] National Radio Astronomy Observatory, 520 Edgemont Road, Charlottesville, VA 22903, USA
[15] Sidrat Research, P.O. Box 73527 RPO Wychwood, Toronto, ON M6C 4A7, Canada
[16] Perimeter Institute for Theoretical Physics, 31 Caroline Street N, Waterloo, ON N25 2YL, Canada
[17] Department of Statistics & Actuarial Science, Simon Fraser University, Burnaby, BC, Canada
Received 2022 November 22; revised 2023 February 6; accepted 2023 February 8; published 2023 March 30

Abstract

The CHIME/FRB project has detected hundreds of fast radio bursts (FRBs), providing an unparalleled population to statistically probe the foreground media that they illuminate. One such foreground medium is the ionized halo of the Milky Way (MW). We estimate the total Galactic electron column density from FRB dispersion measures (DMs) as a function of Galactic latitude using four different estimators, including ones that assume spherical symmetry of the ionized MW halo and ones that imply more latitudinal variation in density. Our observation-based constraints of the total Galactic DM contribution for $|b| \geqslant 30°$, depending on the Galactic latitude and selected model, span 87.8–141 pc cm^{-3}. This constraint implies upper limits on the MW halo DM contribution that range over 52–111 pc cm^{-3}. We discuss the viability of various gas density profiles for the MW halo that have been used to estimate the halo's contribution to DMs of extragalactic sources. Several models overestimate the DM contribution, especially when assuming higher halo gas masses ($\sim 3.5 \times 10^{12}\ M_{\odot}$). Some halo models predict a higher MW halo DM contribution than can be supported by our observations unless the effect of feedback is increased within them, highlighting the impact of feedback processes in galaxy formation.

Unified Astronomy Thesaurus concepts: Galactic radio sources (571); Radio bursts (1339); Circumgalactic medium (1879); Galaxy structure (622); Hot ionized medium (752); Warm ionized medium (1788)

1. Introduction

Our Galactic halo connects the baryon-rich intergalactic medium (IGM) to the disk of the Milky Way (MW). Gas from the halo is a combination of new and recycled material, is a consequence of galactic feedback processes, and represents a galaxy's future star formation fuel. The MW halo contains both neutral and ionized gas, although it is dominated in mass by the latter component, which extends to hundreds of kiloparsecs (Reynolds 1991; Putman et al. 2012).

Meaningful theoretical predictions of the composition and size of the MW halo come from our knowledge of cosmology and galaxy formation theory (for a review, see Putman et al. 2012). In this sense, the total mass and extent of the halo can be used to check our understanding of these topics. Unfortunately, due to the diffuse and hot nature of the ionized halo gas and our position within the MW, the MW halo gas cannot be imaged directly.

Existing indirect constraints for the total amount of hot halo gas have been placed using observations of the ~0.1–1 keV diffuse soft X-ray background, which find typical emission measures (EMs) of $(1.4–3.0) \times 10^{-3}$ cm^{-6} pc (Gupta et al. 2009; Yoshino et al. 2009; Henley et al. 2010; Henley & Shelton 2013). Indirect constraints for the total amount of plasma have also been placed using absorption lines of oxygen

ions in X-ray and far-ultraviolet spectroscopy of active galactic nuclei; however, there are considerably fewer useful sight lines (Gupta et al. 2012; Sakai et al. 2012; Fang et al. 2015). Most of the hot gas detected in X-ray emission is thought to be within a few kiloparsecs of the MW disk (Fang et al. 2006; Yao & Wang 2007), although evidence exists for extended hot halo gas with density on the order of 10^{-5}–10^{-4} cm^{-2} at distances of 50–100 kpc (Sembach et al. 2003; Stanimirović et al. 2006; Grcevich & Putman 2009). More accurate estimates of the total mass of the ionized medium in the halo require a more precise knowledge of the physical properties of this extended ionized gas. Evidence is emerging suggesting more structure within the MW halo gas, although most models previously had assumed spherical symmetry. Yamasaki & Totani (2020) and Ueda et al. (2022) found evidence for a disklike component to the MW halo gas. The gas closest to us (within 50 Mpc) suggests that the hot halo gas cannot be the host of all of the missing baryons (Bregman et al. 2015, 2018). However, Faerman et al. (2017) showed that if the gas density beyond 50 kpc were to flatten, the hot halo gas could account for the missing baryons.

Another constraint on the mass and extent of the plasma in the MW halo comes from radio observations of pulsars in the Large and Small Magellanic Clouds (LMC and SMC; e.g., Ridley et al. 2013). The LMC and SMC are located ∼50 and 60 kpc away, respectively (Pietrzyński et al. 2019; Graczyk et al. 2020), but this distance is only a small fraction of the virial radius of the MW (using the definition of Bryan & Norman 1998, current estimates of the latter are typically between 180 and 250 kpc; Bovy 2015; Cautun et al. 2020; Shen et al. 2022).

The key to the LMC and SMC pulsar-based halo constraint is the significant dispersive effect of ionized gas on radio waves. Precise measurements of arrival times at the top (high frequencies, ν_1) versus bottom (low frequencies, ν_2) of a radio survey's observing band or the detectable emission for short bursts allow for a quantification of the dispersive delay known as the dispersion measure (DM). This effect is mainly due to the electrons along the line of sight and thus approximately (i.e., good to within one part per thousand; see Kulkarni 2020 for an in-depth discussion) proportional to the column density of free electrons,

$$\mathrm{DM} = \int_0^L n_e \, dl, \tag{1}$$

where L is the distance to the source, in this case the pulsars in the LMC or SMC, and n_e is the free electron number density. The DM is determined from observations via the relationship

$$\Delta t = \frac{(e^-)^2}{2\pi m_e c}\left(\frac{1}{\nu_2^2} - \frac{1}{\nu_1^2}\right)\mathrm{DM}, \tag{2}$$

where Δt is the wave arrival time delay between ν_1 and ν_2.[18] The DM is a direct probe of the intervening plasma between observers and radio transients. The radio pulsars within the SMC and LMC set a lower bound on the Galactic DM contribution at their respective distances of 70 ± 3 and 45 ± 1 pc cm^{-3} (Manchester et al. 2006).

The DM is also useful for constraining the plasma within the Galactic disk. One can characterize this medium using pulsars with independent distance measurements, typically through annual parallax, which enables the modeling of the scale height and midplane density of the warm ionized medium (WIM) disk (Cordes & Lazio 2002; Gaensler et al. 2008; Savage & Wakker 2009; Schnitzeler 2012; Yao et al. 2017; Ocker et al. 2020).

Galactic plasma models NE2001 (Cordes & Lazio 2002) and the more recent YMW16 (Yao et al. 2017) include more components than scale height, filling factor, and vertical electron column, in contrast to the other models listed above, but NE2001 and YMW16 are also based on DM measurements of pulsars with independent distance measurements. Both models include components for the thin and thick disk, spiral arms, and local structures like the Local Bubble and the Gum Nebula. The NE2001 model parameters were fit using data from 112 pulsar distances and 269 scattering measurements. The YMW16 used 189 independent pulsar distances and an updated estimate of the WIM disk scale height.[19] Both models have been shown to fail in predicting the DMs of certain populations, like high-latitude pulsars, pulsars in H II regions, and several relatively local pulsars (Chatterjee et al. 2009). Price et al. (2021) gave a comprehensive review and comparison of these two models.

Unfortunately, there are very few known pulsars available to probe significant fractions of the MW halo. One expects to find the highest density of canonical pulsars, remnants of short-lived massive stars, within the disk; hence, historical pulsar surveys most commonly target this area. Typical pulsar emission is also too faint to readily observe at great distances like the edge of the Galaxy or beyond.

Fast radio burst (FRB) DMs are a new way to constrain the total mass and extent of the halo. The class-defining observation of an FRB (Lorimer et al. 2007), FRB 20010724A, caught the attention of astronomers in part because the burst had a DM higher than could be contributed by our Galaxy along that line of sight according to Galactic electron density models like NE2001.

Most observed FRBs have DMs many times what these models estimate can be expected from our Galaxy based on the above models or the measured scale height and average vertical electron column of the MW. In all published instances of precise FRB localizations to date, the FRB is spatially coincident with a galaxy (for a review of host galaxy associations, see Heintz et al. 2020). These associations confirm their extragalactic nature, as the chance coincidence of finding a galaxy that is physically unrelated to the source in their small localization regions is negligible. The FRBs with DMs substantially larger than that maximally predicted by Galactic density models in their line of sight can be assumed to be extragalactic.[20]

We can define the measured DM of an extragalactic FRB as the sum of the following four components:

$$\mathrm{DM} = \mathrm{DM_{disk}} + \mathrm{DM_{halo}} + \mathrm{DM_{cosmic}} + \frac{\mathrm{DM_{host}}}{1+z}, \tag{3}$$

[18] The first term of constants is set to be exactly $1/2.41 \times 10^{-4}$ within CHIME/FRB's pipeline (CHIME/FRB Collaboration 2018).

[19] Yao et al. (2017) argued that scattering measures are generally dominated by a few foreground structures along the line of sight to a pulsar and not the large-scale structure of the Galaxy, so they did not include these measurements in their model. Notably, neither model includes a component for the MW halo.

[20] There have been detections of FRB-like events from within the MW from a known Galactic source, namely, magnetar SGR 1935+2154 (Bochenek et al. 2020; CHIME/FRB Collaboration 2020, 2022). The DM of this burst was consistent with being Galactic according to NE2001 and YMW16.

where the terms refer to the DM contributions from electrons in the MW disk, MW halo, cosmic web, and FRB host galaxy. The first two terms, DM_{disk} and DM_{halo}, when summed, are denoted DM_{Gal}, as they comprise the contribution from the MW in a given line of sight, i.e.,

$$DM_{Gal} = DM_{disk} + DM_{halo}. \quad (4)$$

The DM_{host} likely includes contributions from the halo and disk of the host galaxy and potentially includes a local component around the source of the burst. The DM_{cosmic} includes contributions from the IGM and ionized gas in the Local Group (Prochaska & Zheng 2019) and could include intervening galaxies or galaxy halos along the line of sight to the FRB (Prochaska et al. 2019).

The MW halo contribution was first constrained using a population of FRBs by Platts et al. (2020). After subtracting the DM_{disk} estimated by NE2001 from the total measured DM of each FRB, the authors modeled the excess DM distributions using asymmetric kernel density estimation and set conservative limits of -2 pc cm$^{-3} < DM_{halo} < 123$ pc cm^{-3}. The authors concluded by emphasizing that they expected that a larger sample of FRBs would tighten these constraints.

In this paper, we derive observation-based upper limits of DM_{halo} as a function of Galactic latitude from the most extensive sample of FRBs to date. In Section 2, we outline the extragalactic source sample from the FRB back end of the Canadian Hydrogen Intensity Mapping Experiment (CHIME), which allows us to make direct upper limits of the column density of ionized halo gas without relying on models for DM_{halo}, DM_{cosmic}, and DM_{host}, each of which remain loosely constrained on a population scale. In Section 3, we compare this extragalactic sample with information from Galactic pulsar DMs and show that there is a distinct gap between the extragalactic and Galactic populations. Then, in Section 4, we derive estimates of DM_{Gal} as a function of Galactic latitude, which, when combined with estimates of DM_{disk}, also describe the structure of DM_{halo} as a function of Galactic latitude. We discuss the biases in our data collection in Section 5.1, as well as how these biases could produce the lack of radio pulse detections between our Galactic and extragalactic populations. The uncertainties of our derived models are discussed in Section 5.2.

2. FRB Sample

Our extragalactic FRB sample comes from CHIME/FRB. CHIME is a radio telescope operating over 400–800 MHz (CHIME Collaboration et al. 2022). It is a transit telescope with no moving parts; it observes the sky above it as the Earth rotates. CHIME is located at the Dominion Radio Astrophysical Observatory near Penticton, British Columbia, Canada. The CHIME telescope is comprised of four 20 m $\times$ 100 m, north/south-oriented, semicylindrical parabolic reflectors, each of which has 256 dual-polarization feeds, giving the entire instrument a more than 200 deg^2 field of view. CHIME's FX correlator forms 1024 beams over this large field of view, and the FRB back end searches the beams for radio pulses with durations of $\sim$1 to hundreds of milliseconds, such as pulsars and FRBs (CHIME/FRB Collaboration 2018). For this study, we selected all 93 sources detected by CHIME/FRB through 2021 February that satisfied our selection criteria, namely, having a low measured DM ($<$250 pc cm^{-3}) and high Galactic latitude ($|b| > 30°$). Thirty-four of these FRBs are reported in the first CHIME/FRB catalog (CHIME/FRB Collaboration 2021). We inspected the events for any evidence that they were detected away from the meridian of the telescope (i.e., in a side lobe), as this can result in a given burst's reported position being inaccurate due to imperfect modeling of the inherent side-lobe-beam structure. None of the bursts in our sample show evidence of being side lobe events, but, especially with the lower signal-to-noise ratio bursts, we cannot completely rule out this possibility with intensity data alone.

We define high latitude as those FRBs with a measured absolute Galactic latitude ($|b|$) greater than 30°. We made this selection to avoid contamination in the measured DM by H II regions and other small-scale local structures. At these latitudes, the maximal DM_{Gal} predicted by Galactic free electron density models YMW16 and NE2001 show significantly less scatter in Galactic longitude, a dimension we collapse over in this study. CHIME/FRB's pipeline imposes another selection criterion on our sample. The pipeline only saves intensity data from bursts with measured DMs greater than at least one of YMW16's or NE2001's maximal DM_{disk} estimate in the burst's apparent line of sight. The impact of this pipeline-imposed selection criterion is discussed further in Section 5.1. Our low-DM samples at these latitudes are FRBs with DM $<$ 250 pc cm^{-3} and are chosen because they are the most constraining on DM_{halo}. Most MW halo models typically translate into DM_{halo} predictions of less than 100 pc cm^{-3}, and at Galactic latitudes greater than 30°, DM_{disk} is predicted to be less than 70 pc cm^{-3} according to NE2001, YMW16, and Ocker et al. (2020). Thus, we choose to consider only FRBs with a measured DM of less than 250 pc cm^{-3} to conservatively explore the range within which models predict DM_{Gal}.

Our selected sample includes four repeating sources, one of which, FRB 20200120E, is associated with spiral galaxy M81 and, at 3.6 Mpc away, is the closest known extragalactic FRB source (Bhardwaj et al. 2021; Kirsten et al. 2022). Repeating FRB 20200120E, which we will denote M81R for brevity, is a particularly interesting source for this study, not only because it likely has a low DM_{cosmic} contribution (Kirsten et al. 2022 estimated this contribution to be on the order of 1 pc cm^{-3}) but also because it is located in a globular cluster on the outskirts of M81 (the globular cluster's offset from the center of M81, measured in projection, is approximately 20 kpc). This circumstance means that we expect a negligible DM contribution from the disk of M81. Additionally, we do not expect that a globular cluster would contribute significant amounts of internal dispersion (Freire et al. 2001).

3. Galactic and Extragalactic Comparisons

The extragalactic FRBs with the lowest DMs provide the most constraining upper limits on DM_{Gal}. Figure 1 shows the DMs of all high-latitude and low-DM FRB candidates from CHIME/FRB (triangles) as a function of sin$|b|$. Repeating FRB sources are shown as red triangles, indicating the best-measured latitude and DM considering all published bursts. The FRB with the smallest DM in our current sample is M81R, with DM = 87.8 pc cm^{-3}.

We plot all Galactic pulsars in DM versus Galactic latitude from the Australia Telescope National Facility (ATNF) pulsar catalog[21] (Manchester et al. 2005; light gray stars) and indicate the sources from this sample that have been detected by the

[21] Version 1.64, accessed 2021 March 23; http://www.atnf.csiro.au/research/pulsar/psrcat.

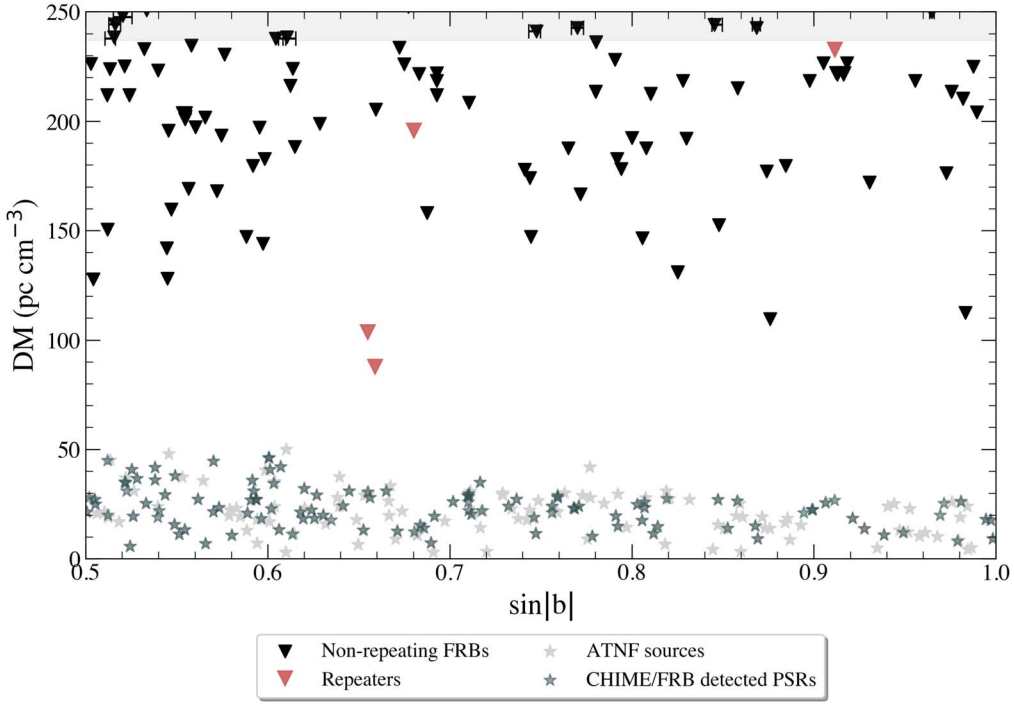

Figure 1. Total measured DM as a function of sin|b| for $|b| \geqslant 30°$ for FRBs detected by CHIME/FRB with DMs less than 250 pc cm^{-3} through 2021 February. Apparent nonrepeating FRBs are represented with black triangles, and repeating FRB sources are represented with red triangles. Galactic sources, namely, pulsars from the ATNF Pulsar Catalogue (light gray; Manchester et al. 2005) and all Galactic sources detected by CHIME/FRB's real-time pipeline (dark gray), are shown (Good et al. 2021). We do not, however, plot sources from lines of sight with very high EMs as measured by Planck (Planck Collaboration et al. 2016a) to avoid higher-than-representative DMs due to contamination by H II regions and other small-scale local structure. Similarly, sources with decl. $< -11°$ are not plotted, as they are outside of CHIME/FRB's field of view, such that longitudinal variation is comparable between the Galactic and extragalactic samples. Representative positional errors are shown for sources in the top gray band. The DM errors of the FRBs are much smaller than the markers, so we do not plot them. A clear gap in DM is visible between the triangles and stars.

real-time CHIME/FRB pipeline (dark gray stars). Additionally, if prepublication pulsars or rotating radio transients (RRATs) - from the pulsar survey scraper[22] have been detected by CHIME/FRB's real-time pipeline through 2021 February, we also include them in this plot (dark gray stars). This addition includes new Galactic sources seen by CHIME[23] (Good et al. 2021; Dong et al. 2022). We exclude ATNF and pulsar survey scraper sources that were detected in lines of sight with EMs above the 95th percentile of the sky as measured by the Planck 2015 astrophysical component separation analysis (Planck Collaboration et al. 2016a). This exclusion is enacted to avoid higher-than-representative DMs due to contamination by H II regions[24] and other small-scale local structure. This cut affects about 30% of pulsars across the sky but does not remove any pulsars from the Galactic latitudes and declinations we consider. The pulsar decl. criterion removes sources that are outside of CHIME's sky coverage (i.e., those with declinations $<-11°$). The pulsars and RRATs all sit below a DM of $\approx$50 pc cm^{-3}, and the highest pulsar or RRAT DMs are largely found at lower sin|b|.

There is a distinct gap in DMs at around 50–87.8 pc cm^{-3} (the exact values depend on the latitude considered, but the gap is not narrower than this in any direction). As discussed more in Section 5.1, for $|b| > 30°$, this gap separates known or suspected Galactic sources and extragalactic FRBs.

[22] https://pulsar.cgca-hub.org/

[23] See https://www.chime-frb.ca/galactic for the most up-to-date catalog.

[24] Most H II are located at low absolute Galactic latitudes, but there are a few that have been observed at Galactic latitudes relevant to our study (Paladini et al. 2003).

4. Analysis

4.1. Basic Methodology

We seek to describe the constraints placed on DM$_{\rm Gal}$ using FRBs as a function of Galactic latitude. Reasonable possibilities for models of DM$_{\rm Gal}$ include those that assume a purely spherical ionized MW halo and those that imply more latitudinal variation in the density of the ionized MW halo. We will fit a model that assumes that DM$_{\rm Gal}$ is constant, a model that assumes that DM$_{\rm halo}$ is constant, and models for DM$_{\rm Gal}$ that take the form of third-order polynomials but still bound the DMs of the FRBs from below. Since measured extragalactic FRB DMs must include the contribution from DM$_{\rm Gal}$ along their line of sight, and each of these models bound the FRB DMs from below, the models represent the upper limits of DM$_{\rm Gal}$ derived when DM$_{\rm cosmic}$ = DM$_{\rm host}$ = 0. We then turn the upper limit models of DM$_{\rm Gal}$ at each latitude into upper limits of DM$_{\rm halo}$ by subtracting the DM$_{\rm disk}$ component as a function of Galactic latitude (b) found by Ocker et al. (2020),

$$\mathrm{DM_{disk}} = \frac{23.5 \pm 2.5}{\sin|b|}\ \mathrm{pc\ cm^{-3}}. \quad (5)$$

4.2. Galactic DM Estimates

In Figure 2, we fit and plot four structure estimates that either strictly or roughly bound the DMs of FRBs from below, since the lowest extragalactic FRB DMs are the most constraining upper limits of the MW halo. The first estimate (red dotted–dashed line in Figure 2) assumes a constant value for the total Galactic contribution DM$_{\rm Gal}$ across the sky. That is, DM$_{\rm Gal}$ =

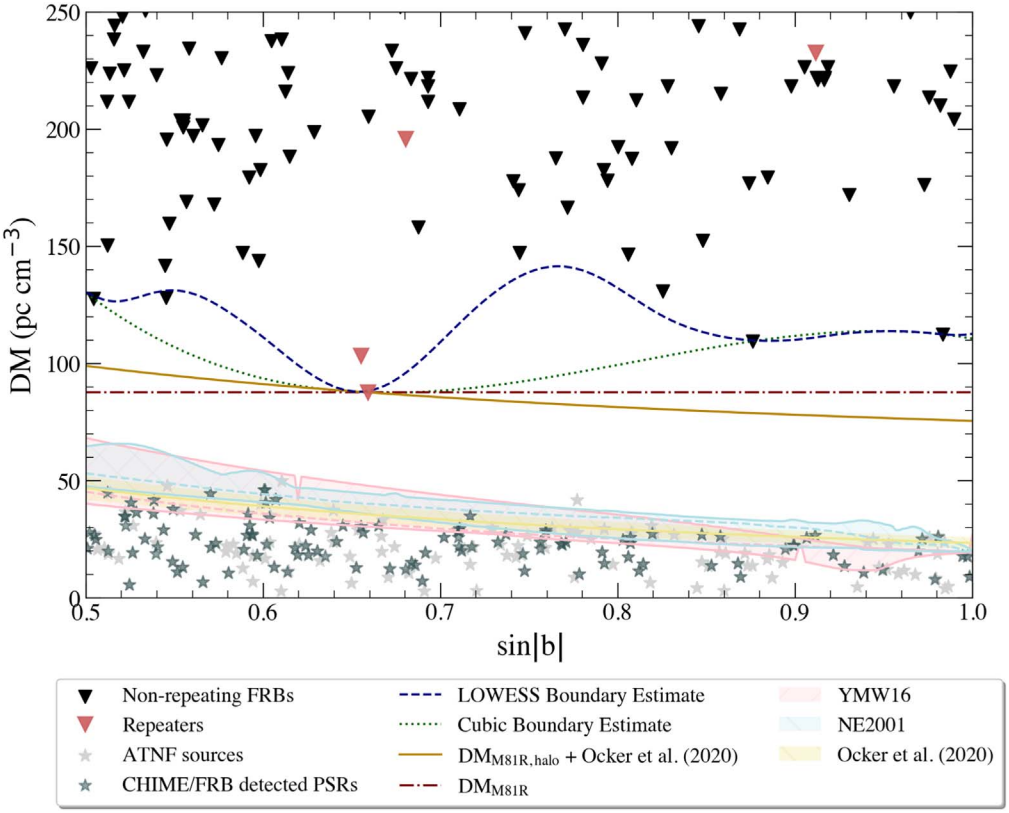

Figure 2. Same as Figure 1, but four simple boundary models of DM_{Gal} are shown, which display the most conservative estimates supported by CHIME/FRB's extragalactic DM sample using different fitting methods and polynomial degrees (see Section 4 for details). Additionally, the total expected Galactic contributions to the DM from the two Galactic free electron density models, NE2001 and YMW16, are plotted in blue and pink, respectively, where the shaded regions bounded by solid lines represent the range in values for lines of sight that vary with Galactic longitude (Cordes & Lazio 2002; Yao et al. 2017). The pink, yellow, and blue dotted lines show the median value of YMW16, Ocker et al. (2020), and NE2001, respectively, at each Galactic latitude. The implied DM of the WIM disk component as a function of Galactic latitude found by Ocker et al. (2020) is shown in yellow.

87.8 pc cm^{-3} for all $|b| \in (30°, 90°)$. This is the measured DM of FRB 20200120E, associated with spiral galaxy M81 (Bhardwaj et al. 2021; Kirsten et al. 2022). Below absolute latitudes of 30°, this model is not supported, as many pulsars have been detected at DMs higher than 87.8 pc cm^{-3}.

The next model (solid yellow line in Figure 2) assumes that the halo has a constant contribution at a given latitude. If DM_{disk} is assumed to be the central value predicted by Ocker et al. (2020) at the latitude of our lowest-DM FRB, likely the most constraining single estimate of DM_{halo}, our observations support a DM_{halo} of no more than 87.8 pc cm^{-3} $-(23.5/\sin(0.64))$ pc cm^{-3} $= 52$ pc cm^{-3}.

Written explicitly,

$$DM_{Gal}(b) = \left(\frac{23.5}{\sin|b|} + 52\right) \text{pc cm}^{-3}. \quad (6)$$

We also fit a model for DM_{Gal} using locally weighted scatterplot smoothing (LOWESS; Cleveland 1979) to the local minimum of the measured FRB DMs (blue dashed line in Figure 2). LOWESS is a method for smoothing a scatterplot in which the fitted value at a given point is the value of a polynomial fit to the data using weighted least squares. The weight is determined by how close the original value is to a local regression so that the weight is large if the proposed value is close to the data and small if not. At each point in $\sin|b|$, we bin all FRB DMs within 5° and select the minimum as the value for that latitude. Using these minima, we fit a LOWESS line with a polynomial degree of 3 and bandwidth of 0.55. A bandwidth of 0.55 means that 55% of the data are considered when smoothing each point. The polynomial degree was chosen because both quadratic and quartic functions predicted behavior near the $|b|$ boundaries that was unphysical, and higher polynomial degrees did not offer a better fit. The DM_{Gal} predictions from this model fall between 88 pc cm^{-3} at $\sin|b| = 0.65$ $(b = 40.^{\circ}8)$ and 111 pc cm^{-3} at $\sin|b| = 0.77$ $(50.^{\circ}1)$. The LOWESS line demonstrates a lot of variation with Galactic latitude. This model is not intended to suggest a physical representation of structure in the halo. Rather, we wanted to demonstrate what conservative upper limits on DM_{Gal} might be reasonable in lines of sight that do not have a particularly constraining FRB DM using more constrained lines of sight nearby in Galactic latitude. These more constrained lines of sight are still relatively sparse at our sample size. This model is likely most appropriate if a conservative estimate is desired.

The final method we apply to model DM_{Gal} as a function of Galactic latitude is polynomial boundary regression. The polynomial boundary regression assumes that the boundary of a given scatterplot can be described by a polynomial and optimizes that polynomial such that it envelopes the data and minimizes the area under its graph (Hall et al. 1998). We computed this estimate assuming a third-degree polynomial using the CRAN package *npbr*[25] (Daouia et al. 2017). For a

[25] https://CRAN.R-project.org/package=npbr

Table 1
Best-fit Parameters Derived for the FRB DM Cubic Boundary Estimate Described in Equation (7)

Coefficient	Value (pc cm^{-3})
x_0	1304
x_1	−4747
x_2	6044
x_3	−2490

cubic polynomial with coefficients defined as

$$\mathrm{DM_{Gal}}(b) = \sum_{i=0}^{3} x_i \sin^i |b|, \quad (7)$$

the best-fit coefficients for our model can be found in Table 1. The cubic boundary regression predicts values for $\mathrm{DM_{Gal}}$ between 87.6 and 130.1 pc cm^{-3} at $\sin|b| = 0.67$ and 0.50, respectively. We plot this model as the green dotted line in Figure 2. When considering the error associated with this estimate of the structure of $\mathrm{DM_{Gal}}$ across Galactic latitude, it is important to consider not only the error in estimation of the fit parameters but also the error introduced by the scatter in $\mathrm{DM_{halo}}$ over Galactic longitudes. We provide pointwise bootstrap errors implied for the fit parameters at doi:10.11570/22.0079. These boundary estimates are summarized for their comparison in Section 5.3 to existing models of $\mathrm{DM_{halo}}$ in Table 2.

We plot $\mathrm{DM_{disk}}$ in Figure 2 as estimated by the two popular free electron density models, NE2001 (Cordes & Lazio 2002) and YMW16 (Yao et al. 2017). We again removed from the data lines of sight with EMs above the 95th percentile of the sky. We remove lines of sight outside of CHIME's sky coverage as in Figure 1 to ensure an appropriate comparison. In Figure 2, NE2001 and YMW16 are shown by blue and pink shaded regions representing the range of maximum Galactic contribution over Galactic longitudes. The dashed lines of the same color located within the shaded regions of both models represent the median value over the relevant Galactic longitude. The implied DM of the WIM disk component as a function of Galactic latitude b found by Ocker et al. (2020), shown in Equation (5), is shown in yellow in Figure 2, where the solid line represents the best-fit model, and the surrounding region represents the model fit uncertainty. The estimated $\mathrm{DM_{disk}}$ from YMW16, NE2001, and Ocker et al. (2020) mostly bound the DMs of the pulsars and RRATs from above. There are a few exceptions where an observed Galactic source is only a few pc cm^{-3} above the largest expected $\mathrm{DM_{disk}}$ from a given model at the relevant Galactic latitude. The FRB DMs are all >30 pc cm^{-3} larger than the largest expected $\mathrm{DM_{disk}}$ from any model.

In summary, our constant Galactic contribution model, constant $\mathrm{DM_{halo}}$ model, LOWESS boundary estimate, and cubic boundary estimate result in high-latitude upper limits on $\mathrm{DM_{Gal}}$ from 87.8 to 141 pc cm^{-3} depending on the model and line of sight considered. By subtracting the $\mathrm{DM_{disk}}$ estimate from Ocker et al. (2020) assuming slab geometry of the disk, we can place upper limits on the $\mathrm{DM_{halo}}$ alone. These constraints range from 52 to 111 pc cm^{-3} depending on the Galactic latitude and model considered.

Table 2
Summary of Our Boundary (Upper Limit) Estimates of $\mathrm{DM_{halo}}$ and $\mathrm{DM_{Gal}}$ as Presented in Section 4

Model	$\mathrm{DM_{Gal}}$ Upper Limit Range (pc cm^{-3})	$\mathrm{DM_{halo}}$ Upper Limit Range (pc cm^{-3})
Constant $\mathrm{DM_{halo}}$	76–99	52
Cubic boundary estimate	87.8−130	52–83
LOWESS estimate	88–141	52–111

Note. The $\mathrm{DM_{halo}}$ upper limits are derived from the $\mathrm{DM_{Gal}}$ estimates by subtracting an estimate of $\mathrm{DM_{disk}}$ from Ocker et al. (2020), shown in Equation (5).

5. Discussion

5.1. Potential Biases in Sample Collection

We explore whether or not the gap in DM between disk pulsars and extragalactic FRBs is physical and caused by the Galactic halo. Note that each measured DM from an FRB source represents an upper limit on $\mathrm{DM_{halo}}$ in that direction, regardless of the astrophysical significance of the lack of intermediate DMs. Our first analysis, which places upper limits across Galactic latitude, does not require the gap to be due to the presence of the halo in order to be a valid constraint.

We first discuss the potential biases contributing to this gap and then explore their effects.

The first potential bias is that CHIME/FRB is less sensitive to radio bursts at low DMs. There are two effects contributing to the lower sensitivity. The first effect for this is, as mentioned in Section 2, our pipeline only saves intensity data for radio pulses with DMs greater than at least one of the maximal $\mathrm{DM_{Gal}}$ estimates of YMW16 and NE2001 in their line of sight. However, as can be seen in Figure 2, for high latitudes, there is still a significant gap in radio pulse DM detections above the DM values where this condition would be relevant.

The second effect that makes CHIME/FRB less sensitive to low-DM bursts is that our wideband radio frequency interference mitigation strategies preferentially remove signals from bright, low-DM events. This likely contributes to the apparent gap. We can quantify the extent of this and other system biases using studies of synthetic injected pulses (for more information on the injection system, see CHIME/FRB Collaboration 2021 and Merryfield et al. 2022). Using the injected pulse system, we find that at excess DMs below 215 pc cm^{-3}, the real-time pipeline recovers roughly 35% of the injected pulses. This number only varies by 2% between the region with a DM excess less than 52 pc cm^{-3} (where we have not detected FRBs) and the region with a DM excess between 52 and 215 pc cm^{-3}, with the pipeline recovering 2% fewer events at the lower DM excess region.

The second bias that could potentially explain this DM gap is a volume effect. The $\mathrm{DM_{cosmic}}$ is believed to be the source of the observed Macquart (DM-z) relation and hence should be a proxy for distance (Macquart et al. 2020; James et al. 2022). In this way, modulo the variation coming from $\mathrm{DM_{Gal}}$ and $\mathrm{DM_{host}}$, we expect to probe smaller volumes of space at lower DMs. However, if we restrict the DM range considered to smaller DMs, and hence volumes, there are fewer possible FRB hosts that could populate this DM region.

The last, and least easily corrected, effect that could contribute to the apparent DM gap is the DM_{host} of the FRBs. This is largely uncertain, and estimates can easily vary from nearly zero (Kirsten et al. 2022) to hundreds of pc cm^{-3} (Tendulkar et al. 2017) depending on their location within and the properties of their host galaxies (see Chawla et al. 2022; Cordes et al. 2022; Niu et al. 2022, for more specific constraints). The majority of FRBs do not have a known host galaxy. In addition, an estimate for DM_{host} could include contributions from ionized gas local to the FRB source depending on the assumed progenitor of the FRB. From the perspective of this analysis, DM_{host} and DM_{halo} contributions are degenerate. Without additional knowledge of their local environments, each of the considered FRBs' total measured DMs (which are less than 250 pc cm^{-3}) could be attributed entirely to a host like that of FRB 20121102A, for example, which has an estimated $DM_{host} \lesssim 342$ pc cm^{-3} (Tendulkar et al. 2017), or that of repeating FRB 20190520B, for which Ocker et al. (2022) inferred a $DM_{host} = 1121^{+89}_{-138}$ pc cm^{-3}.

In the Appendix, we estimate the astrophysical significance of the "gap" by quantifying the likelihood of observing zero events within the gap. The overall conclusion from the conservative probability estimate is that the observed gap in DM is roughly consistent with arising from pipeline biases and volume effects alone. As any extragalactic DM from an FRB represents an upper limit on DM_{halo} in that direction, this does not invalidate the upper limits we have placed as a function of Galactic latitude. Instead, it suggests that through 2021 February, the high-latitude FRB DMs detected by CHIME/FRB are consistent (under the stated assumptions) with the Galactic halo contributing 0 pc cm^{-3} to the total DM of the FRBs. Of course, the upper limit analysis we present supports values from zero to minimally 52 pc cm^{-3} and maximally 111 pc cm^{-3} (depending on the sight line and model selected), favoring no value within that range.

Given that $DM_{halo} = 0$ pc cm^{-3} is supported in our models and the gap analysis, one could argue that our sample is not yet of adequate size or resolution to detect the halo's total mass and extent but rather only constrains it.

5.2. Model Uncertainties and Unmodeled Contributions

There are three main sources of error when describing the boundary of the halo as in Section 4. There is random error in parameter estimation, error due to unmodeled longitudinal variation, and the contribution of DM_{host} and DM_{cosmic}.

As discussed in Section 4 when introducing the cubic boundary estimate of DM_{Gal}, the first source of uncertainty is due to parameter estimation. We resample our original data set of pairs of FRB DMs and latitudes, which were used to fit our DM_{halo} models, 1000 times with replacement (bootstrapping) to estimate pointwise 90% confidence intervals. We show this 90% confidence interval of the cubic boundary estimate of DM_{Gal} as the region bound by solid green lines in Figure 3.

The second source of uncertainty, also discussed in Section 4, is longitudinal variation in DM_{halo}. This variation introduces error in the models, which is unaccounted for (due to the small sample size) in this analysis.

A scatter of 0.3–0.4 dex is seen in both Suzaku (Nakashima et al. 2018) and HaloSat X-ray EM data (Kaaret et al. 2020) of the MW halo. If we knew exactly what fraction of this scatter can be attributed to the fluctuation of the MW halo gas density, it would tell us the approximate scatter of DM_{halo}, as EM is proportional to the path integral of n_e^2, while DM is proportional to the path integral of n_e. It is worth noting that the instrumental limitations of X-ray telescopes are such that these observations are sensitive to only the densest hot gas, whereas the integrated DM_{halo} will include more distant, diffuse gas (Fang et al. 2006; Yao & Wang 2007). As such, one may expect DM_{halo} to have much less scatter. We assume that the upper limit on the fluctuation of DM_{halo} is approximately $\approx$0.2 dex. This also constrains the total amount of longitudinal variation we expect. For each $\sin|b|$, we illustrate in Figure 3 the extent of a 0.2 dex variation around our cubic boundary estimate of DM_{Gal} (the region bounded by solid orange lines; see Section 3 for more information on the cubic boundary estimation).

To investigate the third source of error, that due to each FRB's nonzero and unaccounted-for DM_{cosmic} and DM_{host}, one can study the most constraining FRB sight line, that of M81R. It is exceptional both in being the lowest-DM source in our sample and in being precisely localized within a globular cluster on the outskirts of the halo of M81 (Bhardwaj et al. 2021; Kirsten et al. 2022). In Bhardwaj et al. (2021), the authors discussed the uncertainties in estimating this source's exact DM_{host} and DM_{cosmic} but ultimately concluded a minimal, conservative, expected $DM_{host} + DM_{cosmic} = 15$ pc cm^{-3}.

Even given the conservative nature of the quadrature sum of these three sources of uncertainty, the region does not encompass any of the Galactic sources in our sample. This is indicative of the conservative nature of the upper limits presented in the paper and a nice consistency check for our models.

Given that the source is relatively nearby (so we expect very little DM_{cosmic}) and has essentially no local or disk DM contributing to DM_{host}, it could be argued that this is an edge case of the FRB population, and it would be appropriate to subtract this same lower bound on $DM_{cosmic} + DM_{host} = 15$ pc cm^{-3} from every line of sight. We refrain from making this generalization in our DM_{halo} estimates given that our sample is not universally localized to the precision required to estimate the DM_{host} contribution, nor is there sufficient knowledge about the population of FRB hosts to make a meaningful distribution-based argument. We still demonstrate, however, the magnitude of this minimal expected contamination of $DM_{host} + DM_{cosmic}$ in Figure 3 (the region bounded by a solid blue line).

5.3. Constraints on Existing Halo Models

Our study was motivated by wanting to observationally constrain the gas content of the MW halo to distinguish between different galaxy formation models. We obtain this constraint by comparing the upper limits implied by FRBs to the estimates made by models with different physical assumptions. First, we review these models and compare their estimates to our DM_{halo} boundary estimates. Table 2 summarizes our DM_{halo} boundary (upper limit) estimates from Section 4.

Keating & Pen (2020) computed most of these estimates of DM_{halo} using gas profiles of halo models. Two total masses of the MW halo are considered in each of their estimates, $M_{halo} = 1.5 \times 10^{12}$ and 3.5×10^{12} $M_\odot$. We compare our FRB constraints with the range bounded by the halo model estimates from the lower- and higher-mass scenario.[26] In addition, for

[26] The fraction of ionized gas differs and is specified by each model.

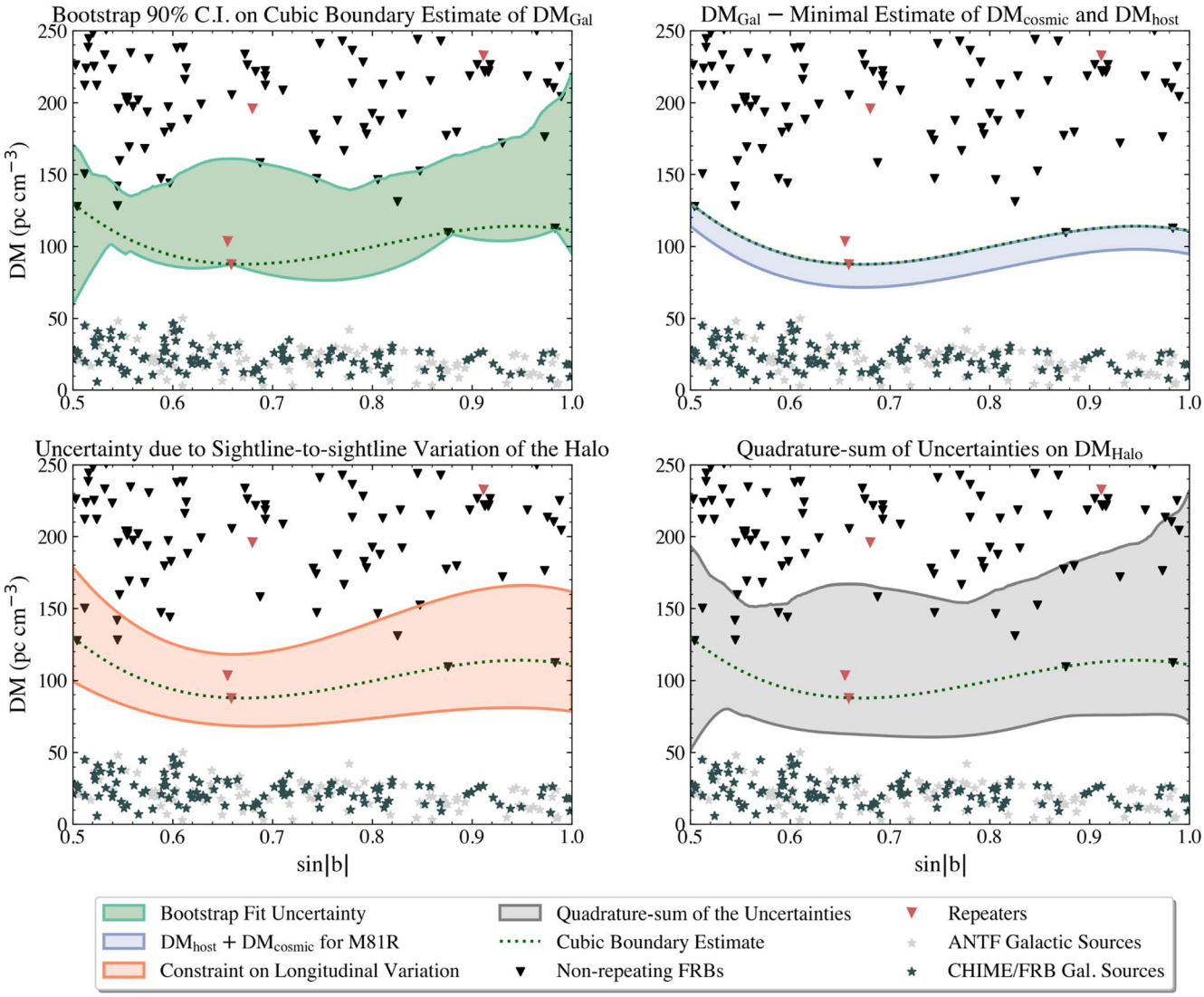

Figure 3. DM vs. sin|b| of radio pulse sources and one of the FRB-derived models of DM_{Gal} from this work to illustrate uncertainties in these models. We plot the cubic boundary estimate of DM_{Gal} derived in Section 4 less the estimate of DM_{disk} from Ocker et al. (2020; green dotted line). All panels are the same as in Figure 1 but with upper limit uncertainty regions demonstrated. These uncertainty regions show where the upper limits on DM_{Gal} could lie, that is, where lines can be drawn such that all DM_{Gal} smaller than that value would be supported by our data. In the top left panel, the green region represents the 90% confidence interval on the cubic boundary estimate via bootstrapping. That is, we remove one of our FRBs at random and reestimate the cubic polynomial boundary as described in Section 4. This process is repeated 1000 times before the 90% pointwise confidence intervals are selected and shown in this panel. In the top right panel, the upper limits we report on DM_{Gal} as a function of Galactic latitude assume that DM_{host} and DM_{cosmic} are zero. For M81R, we have a reasonable estimate of DM_{Gal}, DM_{host}, and DM_{cosmic} given its precise localization (Bhardwaj et al. 2021; Kirsten et al. 2022). We can look at the impact of this assumption using a minimal (conservative) estimate of the $DM_{host} + DM_{cosmic} = 15$ pc cm^{-3} value from M81R. We show the resulting DM_{Gal} (blue region) after removing the implied minimal estimate of contamination by $DM_{host} + DM_{cosmic}$ from our cubic boundary estimate of DM_{Gal}. By removing this value of 15 pc cm^{-3} across the sky, it is assumed that each FRB in the sample has a greater DM_{cosmic} and DM_{host} contribution than M81R, which may be appropriate given the exceptional nature of the M81R sight line (see Section 5.2 for more details). In the bottom left panel, the region bounded by orange lines is a constraint on the longitudinal variation of DM_{halo} at each line of sight, given that Yamasaki & Totani (2020) estimated the scatter of DM_{halo} across the entire sky to be approximately 0.2 dex, and that the variation in longitude must be a subset of the total sight line–to–sight line variation across the sky. Our four models for DM_{Gal} are upper limits that do not account for DM_{cosmic} or DM_{host}. This does not account for spherical geometry; that is, at very high latitudes, we expect the sight line–to–sight line variation to become negligible, as the sky area is also decreasing below spatial scales where we expect the halo plasma to vary. In the bottom right panel, the three sources of uncertainty from the other panels are added in quadrature. These three sources of uncertainty are not independent (for example, some of the uncertainty in the cubic boundary estimate certainly arises from the sight line–to–sight line variation), so this error is larger and hence more conservative than the true combined error.

some of the models, multiple physical scenarios are considered. In this case, which is noted in the brief descriptions of the models that follow, we additionally consider the range in values between these multiple scenarios. We briefly summarize the models included for their comparison to our upper limits.

Navarro et al. (1996) and Mathews & Prochaska (2017). The Navarro–Frenk–White (NFW; Navarro et al. 1996) profile describes well the density profile of virialized dark matter halos in cosmological simulations. A simple model for the baryonic matter is to assume that it traces dark matter near the cosmic ratio ($\Omega_b/\Omega_m \sim 0.2$; Planck Collaboration et al. 2016b) down to 10% of the MW virial radius, in which case the gas density profile (ρ) as a function of distance from the center of the Galaxy (r) can be described using the NFW profile,

$$\rho(r) = \frac{\rho_0}{y(1+y^2)}, \tag{8}$$

where $y = c(r/r_V)$ with concentration c and r_V is the virial radius, and ρ_0 is a characteristic density. This model predicts $\mathrm{DM_{halo}} \approx 300$–$500\ \mathrm{pc\,cm^{-3}}$ and hence was inconsistent with previous observations (Keating & Pen 2020) and remains inconsistent given our observations. This simple model does not account for nonlinear effects facilitated by, e.g., feedback, accretion, and shocks. Mathews & Prochaska (2017) modify the NFW profile with an additional two parameters (y_0, a) based on measurements of O VI absorption in quasar spectra caused by intervening galactic halos:

$$\rho(r) = \frac{\rho_0}{y(y_0 + y)^{2+\alpha}}. \quad (9)$$

This extension to baryonic matter accounts for feedback. We consider (as in Prochaska & Zheng 2019 and Keating & Pen 2020) profiles with $y_0 = 2$ and 4 in the span of this modified NFW (mNFW) profile predicted $\mathrm{DM_{halo}}$ in Figure 4 while keeping $\alpha = 2$ fixed for both cases. In the $y_0 = 2$ case, the profile is disfavored for both of the halo masses considered (i.e., between 1.5 and $3.0 \times 10^{12}\ M_\odot$), as it predicts $\mathrm{DM_{halo}} = 66$–$86\ \mathrm{pc\,cm^{-3}}$, which is higher than the upper limits in most lines of sight of each of our four models. The profile with $y_0 = 4$ remains more plausible for lower masses, as it predicts $\mathrm{DM_{halo}} = 41$–$51\ \mathrm{pc\,cm^{-3}}$.

Maller & Bullock (2004) (MB04). MB04 created their gas density profile by assuming that the halo gas is adiabatic and in hydrostatic equilibrium, taking into account the expectation that the hot gas in halos is prone to fragmentation during cooling due to its thermal instability. The resulting density profile is defined as

$$\rho(r) = \rho_c \left(1 + \frac{3.7}{y}\ln(1 + y) - \frac{3.7}{C_c}\ln(1 + C_c)\right)^{3/2}, \quad (10)$$

where again, $y = c(r/r_V)$. Here ρ_c is a normalization constant set by the assumed gas mass of the halo, and $C_c = c\frac{r_c}{r_V}$ with $r_c = 147$ kpc as assumed by Prochaska & Zheng (2019) and Keating & Pen (2020). All masses considered are compatible, as they are slightly lower than the upper limits given by our observations, as $\mathrm{DM_{halo}}$ is estimated to be 42 and 56 $\mathrm{pc\,cm^{-3}}$ in the low and high halo mass scenarios, respectively. If this model is correct and the mass of the MW halo is within $(1.5, 3.5) \times 10^{12}\ M_\odot$, when this estimate is used in the line of sight of M81R, it would suggest that $\mathrm{DM_{host}}$ (including that from the likely significant fraction of M81's halo that the burst encounters) would need to contribute considerably less DM than the MW halo.

Miller & Bregman (2013) (MB13). MB13 used archival soft X-ray data from XMM-Newton's Reflection Grating Spectrometer to measure O VII Kα. This is used to find the best-fit parameters ($n_0 = 0.46\ \mathrm{cm^{-3}}$, $r_c = 0.35$ kpc, and $\beta = 0.71$) for an underlying spherical density of the hot Galactic halo (n) model of the form

$$n(r) = n_0\left(1 + \frac{r}{r_c}\right)^{-3\beta/2} \quad (11)$$

with the addition of an ambient density component due to ram pressure stripping of $n = 1 \times 10^{-5}\ \mathrm{cm^{-3}}$ out to 200 kpc. As the density profile with the lowest estimated $\mathrm{DM_{halo}}$, this model is not ruled out at these masses. Keating & Pen (2020) estimated the contribution from these as $\approx 6\ \mathrm{pc\,cm^{-3}}$ in the low-mass halo scenario and $\approx 7\ \mathrm{pc\,cm^{-3}}$ in the higher-mass scenario.

Pen (1999) (P99). P99 used an entropy-floor singular isothermal sphere model motivated by observations of the soft X-ray background. In this model, the halo gas is assumed to have two phases, an outer region in which gas traces mass isothermally and an inner region in which the gas has been heated to constant entropy, invoking baryonic feedback. Keating & Pen (2020) considered two cases of the model, one with a heated core radius (r_c) that produces X-ray emission at the limit of the observational constraints of Moretti et al. (2003) and one that maximizes the effect of feedback by choosing r_c equal to the virial radius of the MW. We consider each of these profiles in Figure 4. When $M_{\mathrm{halo}} = 1.5 \times 10^{12}\ M_\odot$ is assumed, and $r_c = 0.34 r_V$ in order to match the X-ray emission, Keating & Pen (2020) estimated $\mathrm{DM_{halo}} \approx 79\ \mathrm{pc\,cm^{-3}}$, which is larger than some of our upper limits and hence largely inconsistent with our observations. When $M_{\mathrm{halo}} = 3.5 \times 10^{12}\ M_\odot$ and $r_c = 0.86 r_V$ (predicted $\mathrm{DM_{halo}} = 34\ \mathrm{pc\,cm^{-3}}$), the measurements are consistent with our observations. Similarly, in either the high- ($M_{\mathrm{halo}} = 3.5 \times 10^{12}\ M_\odot$) or low- ($M_{\mathrm{halo}} = 1.5 \times 10^{12}\ M_\odot$) mass scenario, when the heated core radius r_c is set equal to r_V ($\mathrm{DM_{halo}} = 28$ and 21 $\mathrm{pc\,cm^{-3}}$ for the high- and low-mass scenario, respectively), the results are consistent with our observations.

Voit (2019) (V19). V19 constructed a model for the halo, called the pNFW model, that assumes a confining gravitational potential with a constant circular velocity at small radii. At larger radii, the circular velocity profile is assumed to decline like that of an NFW halo with scale radius $r_{s,\ \mathrm{NFW}}$. These two profiles are joined continuously at a radius of $2.163 r_{s,\ \mathrm{NFW}}$. The author provided a table of formula coefficients as a function of input halo mass for the resultant density profile. In this model, only the lower halo mass scenarios are consistent with all of our lines of sight, since the model estimates $\mathrm{DM_{halo}} = 24$–$84\ \mathrm{pc\,cm^{-3}}$ for MW halo masses between 1.5 and $3.0 \times 10^{12}\ M_\odot$.

In addition to the estimates derived by Keating & Pen (2020) from the above density profiles, we compare our observations to the following estimates for $\mathrm{DM_{halo}}$.

Yamasaki & Totani (2020) (YT20). YT20 modeled the MW halo with a spherical component of isothermal gas in hydrostatic equilibrium and a disklike hot gas component to reproduce the directional dependence of X-ray EM observed by Nakashima et al. (2018). They presented an analytic formula for $\mathrm{DM_{halo}}$ that we plot as a function of Galactic latitude while representing the longitudinal variation as a span in the left panel of Figure 4. At $|b| > 30°$, this model predicts a $\mathrm{DM_{halo}}$ of between 29 and $68\ \mathrm{pc\,cm^{-3}}$ depending on the line of sight considered. As can be seen in Figure 4, at each b, the minimum and median values lie below our cubic boundary estimate of $\mathrm{DM_{halo}}$, and in most cases, the maximum $\mathrm{DM_{halo}}$ prediction also lies below our model. At the sky position of M81R, YT20 predicted $\mathrm{DM_{halo}} \approx 30.5\ \mathrm{pc\,cm^{-3}}$. Our constraint is $\mathrm{DM_{halo}} < 52\ \mathrm{pc\,cm^{-3}}$ for all boundary models; hence, we find that the YT20 model is consistent with our FRB observations.

Dolag et al. (2015) (D15). D15 performed cosmological simulations of an MW-like galactic halo including hot thermal electrons in order to estimate $\mathrm{DM_{halo}}$. Their probable values for $\mathrm{DM_{halo}}$, depending on which inner radius one expects from the edge of the Galactic disk, range over ≈ 24–$67\ \mathrm{pc\,cm^{-3}}$. This

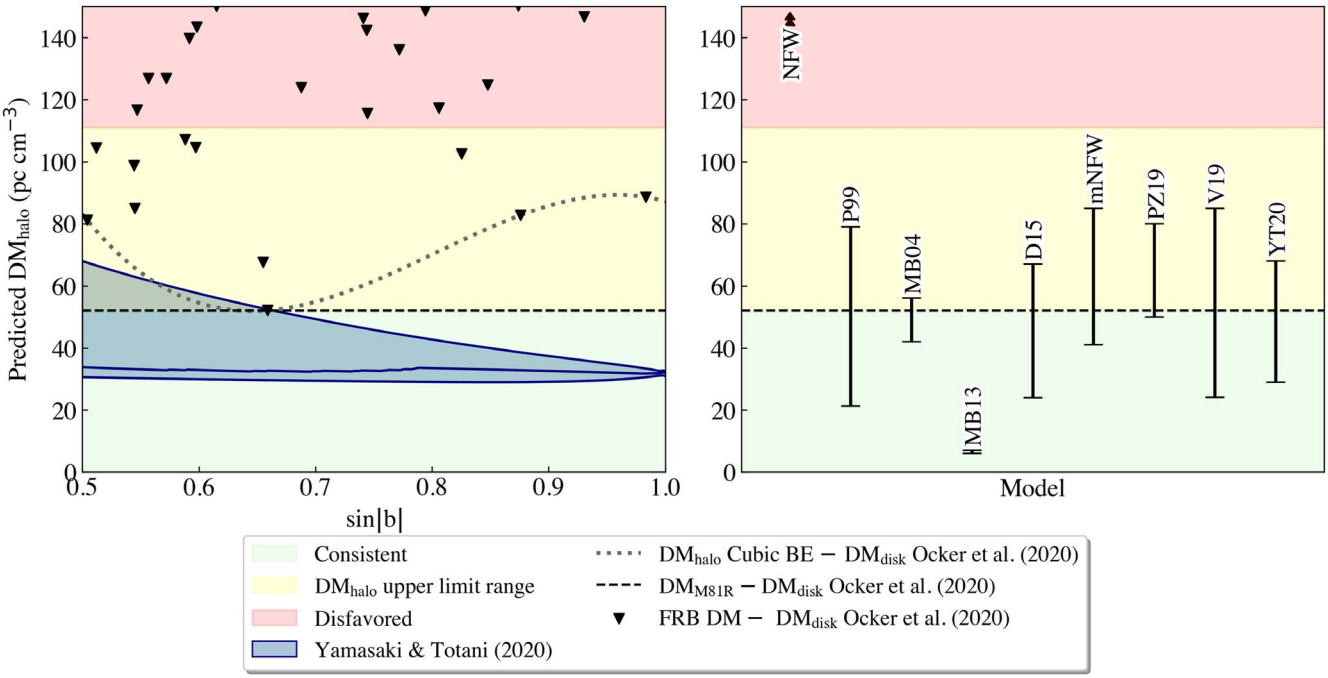

Figure 4. Left panel: comparisons between the predicted DM_{halo} vs. Galactic latitude of the upper limits derived from FRBs in this work and Yamasaki & Totani (2020). The red region shows values of DM_{halo} that are contradictory to our observations, as they are higher than our predictions for DM_{halo} at all latitudes. The yellow region shows the span of our DM_{halo} model predictions (52–111 pc cm^{-3}) and hence denotes DM_{host} values where the models are not strictly ruled out but seem less likely than models in the green region due to the conservative upper limit nature of our result. The dashed line shows the DM of the M81 repeater (Bhardwaj et al. 2021) minus the mean prediction for DM_{disk} at the source's latitude from Ocker et al. (2020) assuming a slab geometry. Black triangles represent the Galactic latitude and excess DM of FRBs in our data set, where excess DM is defined here as the true DM minus DM_{disk} as estimated by Ocker et al. (2020) assuming a slab geometry (Equation (5)). We also plot the cubic boundary estimate of DM_{Gal} derived in Section 4 less the estimate of DM_{disk} from Ocker et al. (2020; gray dotted line). Yamasaki & Totani (2020) made predictions for the halo contribution as a function of Galactic latitude, and we show these predictions in the blue region, where the span represents the range of predictions over all Galactic longitudes in CHIME/FRB's field of view. The three solid blue lines indicate the minimum, median, and maximum DM_{halo} at each sin|b| for all considered l. At l, $b = 142.^{\circ}19, +41.^{\circ}22$, the position of M81R, the DM_{halo} prediction from YT20 is 30.6 pc cm^{-3}. Right panel: comparisons between the predicted DM_{halo} for a selection of popular halo models (ordered by publication date) and the upper limits derived from FRBs in this work. The acronyms for the models are defined along with their brief descriptions in Section 5.3. For the MB13, V19, MB04, and NFW models, the ranges represent the different input masses for the MW halo spanning (1.5–3.5) $\times 10^{12}\,M_{\odot}$ (Keating & Pen 2020). The range for P99 includes three values of the heated core radius. The range in YT20 represents the longitudinal variation in the high-latitude portion of the model.

range, particularly for the larger radii of the edge of the Galactic disk, remains highly relevant and agrees well with our observations, as does the commonly cited representative halo electron column estimate of $DM_{halo} = 30$ pc cm^{-3} selected by the authors. This representative value assumes integration radii beginning 17 kpc from the Galactic center, the maximal extent of NE2001 that was used by Dolag et al. (2015) to model DM_{disk}.

Prochaska & Zheng (2019) (PZ19). PZ19 looked at tracers of the "hot" ($T \sim 10^6$ K) and "cool" ($T \sim 10^4$ K) components of the halo gas. These tracers, namely, observations of O VI and O VII absorption (Fang et al. 2015), Si II and Si III (Richter et al. 2017), and high-velocity clouds (HI4PI Collaboration et al. 2016), are combined with hydrostatic models of the halo to estimate $DM_{halo} = 50$–80 pc cm^{-3} integrated to 200 kpc. This is within the upper limit range of our various models, but most of the range is above the excess DM of M81R (see also Bhardwaj et al. 2021).

We compare our DM_{halo} boundary estimates and upper limits to estimates of DM_{halo} implied by various models in Figure 4. The red region in Figure 4 shows the DM range that cannot be supported by our observations regardless of model chosen or line of sight. Within the yellow region, we show the DM range that encompasses all upper limits from our models, ranging between 52 and 111 pc cm^{-3}. We highlight the excess DM of M81R (FRB 20200120E; Bhardwaj et al. 2021), which is the lowest extragalactic DM in our sample, with the black dotted line.

To summarize, the NFW profile can be unambiguously ruled out (as was previously known by, e.g., Fang et al. 2013 and Pen 1999), and MB13, YT20, and D15 are consistent with our observations. In the case of mNFW, MB04, and V19, the models are mildly in tension with our observations for the high MW halo mass considered ($3.5 \times 10^{12}\,M_{\odot}$) but not for the low-mass ($1.5 \times 10^{12}\,M_{\odot}$) scenario. Similarly, for P99, the model is supported only when the heated core radius is set at the virial radius or the MW halo is assumed to be of lower mass. The majority of the DM_{halo} range proposed by PZ19 is higher than our estimates but remains possible in the scenario where there is significant DM_{halo} scatter in the sky, as acknowledged for the M81R sight line (Bhardwaj et al. 2021).

Baryonic feedback processes and their overall effect are still relatively uncertain in galaxy formation; however, it is interesting to note that both the NFW/mNFW model and P99's models flip from inconsistent with our observations to consistent when consideration for the effect of feedback is increased. The cosmological simulation of D15 that results in a DM_{halo} estimate that is in great agreement with our observations also accounts for the energy released in explosions of massive stars as supernovae, a type of baryonic feedback, and for feedback from active galactic nuclei.

6. Conclusions

We explore the constraints on the total Milky Way (MW) dispersion measure (DM), as well as the MW halo DM using CHIME/FRB's large, extragalactic, fast radio burst (FRB) source population. This sample of DM measurements offers a unique opportunity to constrain the distribution of the Galactic plasma and estimate the MW halo DM contribution upper limits as a function of Galactic latitude. The observation-based high-latitude upper limits on the Galactic DM contribution range over 87.8–141 pc cm^{-3} depending on the chosen model and the Galactic latitude of interest. Subtracting estimates of the disk contribution from Ocker et al. (2020), we derive upper limits on the MW halo DM contribution ranging over 52–111 pc cm^{-3}. These results agree with the recently reported constraint of $\mathrm{DM_{halo}} \leqslant 47.3$ pc cm^{-3} along the line of sight toward FRB 20220319D, located at a comparatively low Galactic latitude of $b \sim +9.^{\circ}1$ (Ravi et al. 2023).

Although there is a DM gap between Galactic and extragalactic radio pulses, assuming the rate at which FRB sources are detected can be described using Poisson statistics, and, using measured population statistics from the first CHIME/FRB catalog, we find that this lack of intermediate DM radio sources is compatible with having arisen from volume effects and pipeline bias alone. The presence of the gap is therefore not evidence of a $\mathrm{DM_{halo}}$ contribution that is nonzero.

Our constraints on the MW halo DM contribution seem in tension with most popular estimates of $\mathrm{DM_{halo}}$ (e.g., Maller & Bullock 2004; Mathews & Prochaska 2017; Voit 2019) when assuming an MW halo mass of $3.5 \times 10^{12}\ M_{\odot}$, with the exception of Miller & Bregman (2013) and Pen (1999). In part, this tension arises because our estimates are necessarily an overestimate of the true value, as we do not estimate and remove DM contributions from the intergalactic medium or host galaxy of each FRB. If we assume a lower MW halo mass estimate of of $1.5 \times 10^{12}\ M_{\odot}$, our constraints agree with more models, including those proposed by Maller & Bullock (2004), Mathews & Prochaska (2017), and Voit (2019). The estimates of the MW halo DM contribution produced by Dolag et al. (2015) using cosmological simulations of an MW-like galactic halo are supported by our observations. So too is the MW halo model of Yamasaki & Totani (2020), which combines a spherical isothermal gas component and a disklike hot gas component. The majority of the $\mathrm{DM_{halo}}$ range proposed by PZ19 is higher than our estimates but remains possible in a scenario where there is significant $\mathrm{DM_{halo}}$ scatter in the sky, as acknowledged for the M81R sight line (Bhardwaj et al. 2021). For some models, these results seem to emphasize the importance of the role of baryonic feedback in Galaxy formation.

While many models of the density of the halo gas invoke strict or quasi-spherical symmetry, one expects the ionized gas in the Local Group to be ellipsoidal, extended from our Galaxy toward M31 due to the inflows, outflows, and tidal interactions between our Galaxy and M31 (Bregman & Lloyd-Davies 2007). Simulation work (Nuza et al. 2014) also finds evidence for this gas excess between a pair of galaxies resembling M31 and the MW compared to another random line of sight. In searches for an excess in DM from FRBs that intersect the dark matter halos of other galaxies, Connor & Ravi (2022) found a higher excess DM in these lines of sight than expected from diffuse gas surrounding isolated galaxies. The authors suggested that this DM excess is potentially due to ionized media in galaxy groups, including the Local Group. Wu & McQuinn (2022) presented a similar analysis but introduced a weighted-stacking scheme that minimizes the effect of the variance of the observed DM distribution and derives a significance for the result that is lower than that found by Connor & Ravi (2022; probability >0.99 versus >0.68 to >0.95). We plan to repeat our study observed in two dimensions (i.e., producing a sky map) once the known FRB population has roughly doubled. This 2D map will allow us to search for evidence of asymmetries in the Galaxy or such an ellipsoidal halo gas distribution that is extended by interactions with our Galaxy group, expected to be dominated by interactions with M31.

We thank Jo Bovy, Stanislav Volgushev, and Jeremy Webb for discussions vital to preparing this work. We are also grateful to the referee for the very thoughtful and constructive comments.

A.M.C. is funded by an NSERC Doctoral Postgraduate Scholarship. M.B. is a McWilliams Fellow. The Dunlap Institute is funded through an endowment established by the David Dunlap family and the University of Toronto. B.M.G. acknowledges the support of the Natural Sciences and Engineering Research Council of Canada (NSERC) through grant RGPIN-2022-03163 and of the Canada Research Chairs program. G.M.E. acknowledges funding from NSERC through Discovery Grant RGPIN-2020-04554 and U of T through the Connaught New Researcher Award. V.M.K. holds the Lorne Trottier Chair in Astrophysics & Cosmology, a Distinguished James McGill Professorship, and receives support from an NSERC Discovery grant (RGPIN 228738-13), an R. Howard Webster Foundation Fellowship from CIFAR, and the FRQNT CRAQ. K.W.M. holds the Adam J. Burgasser Chair in Astrophysics and is supported by an NSF grant (2008031). A.P.C. is a Vanier Canada Graduate Scholar. F.A.D. is supported by the UBC Four Year Fellowship. C.L. was supported by the U.S. Department of Defense (DoD) through the National Defense Science & Engineering Graduate Fellowship (NDSEG) Program. A.P. is funded by an Ontario Graduate Scholarship. A.B.P. is a McGill Space Institute (MSI) Fellow and a Fonds de Recherche du Quebec—Nature et Technologies (FRQNT) postdoctoral fellow. Z.P. is a Dunlap Fellow. The National Radio Astronomy Observatory is a facility of the National Science Foundation operated under cooperative agreement by Associated Universities, Inc. S.M.R. is a CIFAR Fellow and supported by NSF Physics Frontiers Center awards 1430284 and 2020265. K.S. is supported by the NSF Graduate Research Fellowship Program. The FRB research at UBC is supported by an NSERC Discovery Grant and the Canadian Institute for Advanced Research. D.C.S. acknowledges the support of the Natural Sciences and Engineering Research Council of Canada (NSERC), RGPIN-2021-03985. We acknowledge that CHIME is located on the traditional, ancestral, and unceded territory of the Syilx/Okanagan people. We are grateful to the staff of the Dominion Radio Astrophysical Observatory, which is operated by the National Research Council of Canada. CHIME is funded by a grant from the Canada Foundation for Innovation (CFI) 2012 Leading Edge Fund (project 31170) and contributions from the provinces of British Columbia, Québec, and Ontario. The CHIME/FRB Project is funded by a grant from the CFI 2015 Innovation Fund (project 33213), contributions from the

provinces of British Columbia and Québec, and the Dunlap Institute for Astronomy and Astrophysics at the University of Toronto. Additional support was provided by the Canadian Institute for Advanced Research (CIFAR), McGill University, and the McGill Space Institute thanks to the Trottier Family Foundation and the University of British Columbia.

Appendix
Quantitative Analysis of the DM Gap

Given the biases discussed in Section 5.1, in this Appendix we will answer the question "Is this gap astrophysical?" or, equivalently, "Does one need more than volume and selection effects to explain this gap?" We do not assert what fraction of the gap can be attributed to $\mathrm{DM_{halo}}$ and $\mathrm{DM_{host}}$ accordingly. To derive the astrophysical significance, we will quantify the likelihood of observing zero events within the "gap," given the observation of 93 FRB sources in the remaining DM range of our sample and considering only the volume and pipeline biases. In order to estimate this likelihood, we make some simplifying assumptions, and we highlight these assumptions as they appear in the derivation. We show at the end of the section that ultimately, these assumptions result in a conservative estimate.

First, we define $\mathrm{DM}-\mathrm{DM_{disk}}$ as the excess DM and assume that it is contributed solely by the IGM. That is, we are assuming that there is no contribution from the MW halo ($\mathrm{DM_{halo}} = 0\ \mathrm{pc\,cm^{-3}}$) or the host galaxy ($\mathrm{DM_{host}} = 0\ \mathrm{pc\,cm^{-3}}$). If we assume that both are zero, and we know that in a given line of sight, the $\mathrm{DM_{cosmic}}$ is proportional to distance (d) and distance is proportional to redshift (z),[27] we are essentially extending the volume in which FRB sources can exist right to the edge of our MW WIM disk. We can estimate the relative rate of FRBs between two volumes using the fluence distribution (commonly referred to as $\log(N)/\log(F)$) of FRBs. We will compare the relative rate of FRBs in the DM gap (excess DMs [0, 52) $\mathrm{pc\,cm^{-3}}$) and in the rest of the sample, which spans excess DMs from [52, 215] $\mathrm{pc\,cm^{-3}}$.

To simplify, assume that FRBs are standard candles; that is, each burst has equal intrinsic energy. The number of FRBs (N) contained in a given spherical volume of radius d is

$$N \propto F^{\alpha} \propto (d^{-2})^{\alpha}, \tag{12}$$

where F is the FRB fluence, d is distance, and α is a power-law index for the cumulative fluence distribution ($\alpha < 0$). For a nonevolving population in Euclidean space, one expects $\alpha = -3/2$, and this is in agreement with the $\alpha = -1.40 \pm 0.11(\mathrm{stat.})^{+0.06}_{-0.09}(\mathrm{sys.})$ measured by CHIME/FRB when including bursts at all DMs/distances in the first FRB catalog (CHIME/FRB Collaboration 2021). At small d, where space is approximately Euclidean, we can assume $d \propto z$ and hence

$$N(<z) \propto z^{-2\alpha}. \tag{13}$$

Now compare the ratio of the volume in which we detect no FRBs (the gap, v_1) and the volume containing our FRB sample (v_2). We can estimate the redshifts at the DM excesses that define our volumes of interest (52 and 215 $\mathrm{pc\,cm^{-3}}$) as in Macquart et al. (2020), who assumed cosmological parameters as measured by Planck Collaboration et al. (2016b). The expected relation between $\mathrm{DM_{cosmic}}$ and redshift results in redshift estimates of 0.06 at 52 $\mathrm{pc\,cm^{-3}}$ and 0.23 at 215 $\mathrm{pc\,cm^{-3}}$. These redshift estimates have uncertainty due to scatter within the IGM on the order of the estimates (0.04 and 0.11 for the first and second volume boundary, respectively) according to the 90% confidence interval on the fit of the $\mathrm{DM_{cosmic}}$–z. However, we simply select the central value of the redshift estimate to define our boundaries and discuss the effect of the scatter in the IGM on this calculation at the end of this section.

We expect the ratio of the number of sources detected in the first and second volumes to be

$$\frac{N_{\mathrm{FRBs},v_1}}{N_{\mathrm{FRBs},v_2}} = \frac{N_{\mathrm{FRBs}}(z \in [0, 0.06))}{N_{\mathrm{FRBs}}(z \in [0, 0.23] - N \in [0, 0.06))} \tag{14}$$

$$= \frac{z_1^{-2\alpha}}{z_2^{-2\alpha} - z_1^{-2\alpha}} \tag{15}$$

$$= \frac{1}{\left(\frac{z_2}{z_1}\right)^{-2\alpha} - 1}, \tag{16}$$

where N_{FRBs} describes the number of detectable FRBs in a given volume or redshift range, and $z_1 = 0.06$ and $z_2 = 0.23$ are the redshifts that define the boundaries of the two volumes of interest (v_1 and v_2, respectively).

Finally, we must account for the sensitivity of CHIME/FRB to radio pulses in the DM range considered. We correct for this effect using information from CHIME/FRB's synthetic signal injection system. For injected FRB signals with excess DM $\in$ [0, 52) and $\in$[52, 250], the fraction of detected events (μ) is $\mu_{v_1} = 0.346$ and $\mu_{v_2} = 0.366$, respectively. Hence, we adjust Equation (16) to account for this bias,

$$\frac{N_{\mathrm{det},v_1}}{N_{\mathrm{det},v_2}} = \frac{\mu_{v_1} N_{\mathrm{FRBs}\ v_1}}{\mu_{v_2} N_{\mathrm{FRBs}\ v_2}}, \tag{17}$$

$$= \frac{\mu_{v_1}}{\mu_{v_2}} \frac{1}{\left(\frac{z_2}{z_1}\right)^{-2\alpha} - 1}, \tag{18}$$

where N_{det} is the number of FRBs we expect CHIME/FRB's real-time pipeline to detect. We only use the FRBs that were detected while the CHIME/FRB pipeline was in the configuration these injections are intended to gauge, leaving us with 83 of our sample 93 FRBs. The other 10 FRBs were detected after 2020 November, when a significant change was implemented in our real-time dedispersion algorithm.

Since we have measured a nonzero N_{det,v_2}, we estimate the expected N_{det,v_1} in the same time frame. Treated as a rate, we can then use Poisson statistics to describe the likelihood of our observation of zero events in volume 1 under our initial assumptions,

$$N_{\mathrm{det},v_1} = \frac{\mu_{v_1}}{\mu_{v_2}} \frac{N_{\mathrm{det},v_2}}{\left(\frac{z_2}{z_1}\right)^{-2\alpha} - 1}. \tag{19}$$

The probability of detecting no events given a rate of N_{det,v_1}, assuming that FRB source detection can be modeled as a Poisson process, is

$$P(\text{no events} \mid \text{rate} = N_{\mathrm{det},v_1}) = e^{-N_{\mathrm{det},v_1}},$$

[27] This can only be assumed for $z \ll 1$, where space is approximately Euclidean.

where P is the likelihood of the observation.

The probability of obtaining zero events in volume 1 under the null hypothesis of there being no astrophysical DM gap is therefore

$$P = \exp\left[-\frac{\mu_{v_1}}{\mu_{v_2}}\frac{N_{\mathrm{det},v_2}}{\left(\frac{z_2}{z_1}\right)^{-2\alpha} - 1}\right] \tag{20}$$

$$= 0.24. \tag{21}$$

Hence, under these assumptions, the resulting likelihood suggests that the lack of FRB detections in the first volume, considering the number of FRBs detected in the second volume, is consistent with being due to pipeline biases and volume effects alone.

If we look at the assumptions that we have made, we find that this likelihood is quite conservative (i.e., likely an overestimate; hence, we expect to see zero FRBs in this region due to volume and selection effects alone less frequently than 24% of the time if we could repeat the experiment again and again). The assumption that FRBs are standard candles predicts fewer low-fluence bursts compared to the true underlying luminosity distribution as seen in the first CHIME/FRB catalog (CHIME/FRB Collaboration 2021), as well as in observations of repeaters (e.g., Li et al. 2021; Lanman et al. 2022). As volume 1 is closer than volume 2, the omission of these low-fluence bursts would decrease the number of detectable bursts per unit volume more in volume 1 than in volume 2. That is, if there were a population of intermediate-fluence FRBs, there should be bursts that are detectable in volume 1 and not volume 2. Hence, we can safely assume that the fraction of detected bursts in volume 1 compared to volume 2, and the true rate, would be larger than what we estimate. This underestimation of the rate will overestimate the likelihood of our observation and hence is a conservative estimate.

In CHIME/FRB Collaboration (2021), the authors investigated the DM–distance relation by splitting the FRB sample into "low DM" (100–500 pc cm^{-3}) and "high DM" (above 500 pc cm^{-3}) and measuring the α for the subsets. One might believe, then, a more appropriate α to be used would be that measured by CHIME/FRB Collaboration (2021), who inferred $\alpha = -0.95 \pm 0.15(\mathrm{stat})^{+0.06}_{-0.19}(\mathrm{sys})$ for events with DMs of 100–500 pc cm^{-3}. However, since we have assumed a standard candle luminosity function, it is not appropriate to use this α value.

Additionally, when we estimate the redshifts that correspond to $\mathrm{DM_{cosmic}} = 52,\ 215$ pc cm^{-3}, hence defining our volume boundaries, we do not consider the uncertainty presented by Macquart et al. (2020). These uncertainties represent the 90% confidence intervals on the fit of $\mathrm{DM_{cosmic}}$ versus redshift (DM $-z$), accounting for scatter within the IGM (cosmic structure). However, as above, this variance is more likely to result in additional FRBs being detected in the first volume, so our estimate remains conservative.

ORCID iDs

Amanda M. Cook https://orcid.org/0000-0001-6422-8125
Mohit Bhardwaj https://orcid.org/0000-0002-3615-3514
B. M. Gaensler https://orcid.org/0000-0002-3382-9558
Paul Scholz https://orcid.org/0000-0002-7374-7119
Gwendolyn M. Eadie https://orcid.org/0000-0003-3734-8177
Alex S. Hill https://orcid.org/0000-0001-7301-5666
Victoria M. Kaspi https://orcid.org/0000-0001-9345-0307
Kiyoshi W. Masui https://orcid.org/0000-0002-4279-6946
Alice P. Curtin https://orcid.org/0000-0002-8376-1563
Fengqiu Adam Dong https://orcid.org/0000-0003-4098-5222
Emmanuel Fonseca https://orcid.org/0000-0001-8384-5049
Antonio Herrera-Martin https://orcid.org/0000-0002-3654-4662
Jane Kaczmarek https://orcid.org/0000-0003-4810-7803
Adam E. Lanman https://orcid.org/0000-0003-2116-3573
Mattias Lazda https://orcid.org/0000-0002-5857-4264
Calvin Leung https://orcid.org/0000-0002-4209-7408
Bradley W. Meyers https://orcid.org/0000-0001-8845-1225
Daniele Michilli https://orcid.org/0000-0002-2551-7554
Ayush Pandhi https://orcid.org/0000-0002-8897-1973
Aaron B. Pearlman https://orcid.org/0000-0002-8912-0732
Ziggy Pleunis https://orcid.org/0000-0002-4795-697X
Scott Ransom https://orcid.org/0000-0001-5799-9714
Mubdi Rahman https://orcid.org/0000-0003-1842-6096
Ketan R. Sand https://orcid.org/0000-0003-3154-3676
Kaitlyn Shin https://orcid.org/0000-0002-6823-2073
Kendrick Smith https://orcid.org/0000-0002-2088-3125
Ingrid Stairs https://orcid.org/0000-0001-9784-8670
David C. Stenning https://orcid.org/0000-0002-9761-4353

References

Bhardwaj, M., Gaensler, B. M., Kaspi, V. M., et al. 2021, ApJL, 910, L18
Bochenek, C. D., Ravi, V., Belov, K. V., et al. 2020, Natur, 587, 59
Bovy, J. 2015, ApJS, 216, 29
Bregman, J. N., Alves, G. C., Miller, M. J., & Hodges-Kluck, E. 2015, JATIS, 1, 045003
Bregman, J. N., Anderson, M. E., Miller, M. J., et al. 2018, ApJ, 862, 3
Bregman, J. N., & Lloyd-Davies, E. J. 2007, ApJ, 669, 990
Bryan, G. L., & Norman, M. L. 1998, ApJ, 495, 80
Cautun, M., Benítez-Llambay, A., Deason, A. J., et al. 2020, MNRAS, 494, 4291
Chatterjee, S., Brisken, W. F., Vlemmings, W. H. T., et al. 2009, ApJ, 698, 250
Chawla, P., Kaspi, V. M., Ransom, S. M., et al. 2022, ApJ, 927, 35
CHIME/FRB Collaboration 2018, ApJ, 863, 48
CHIME/FRB Collaboration 2020, Natur, 587, 54
CHIME/FRB Collaboration 2021, ApJS, 257, 59
CHIME/FRB Collaboration 2022, ATel, 15681, 1, https://www.astronomerstelegram.org/?read=15681
CHIME Collaboration, Amiri, M., Bandura, K., et al. 2022, ApJS, 261, 29
Cleveland, W. S. 1979, J. Am. Stat. Assoc., 74, 829
Connor, L., & Ravi, V. 2022, NatAs, 6, 1035
Cordes, J. M., & Lazio, T. J. W. 2002, arXiv:astro-ph/0207156
Cordes, J. M., Ocker, S. K., & Chatterjee, S. 2022, ApJ, 931, 88
Daouia, A., Laurent, T., & Noh, H. 2017, J. Stat. Softw., 79, 1
Dolag, K., Gaensler, B. M., Beck, A. M., & Beck, M. C. 2015, MNRAS, 451, 4277
Dong, F. A., Crowter, K., Meyers, B. W., et al. 2022, MNRAS, submitted (arXiv:2210.09172)
Faerman, Y., Sternberg, A., & McKee, C. F. 2017, ApJ, 835, 52
Fang, T., Bullock, J., & Boylan-Kolchin, M. 2013, ApJ, 762, 20
Fang, T., Buote, D., Bullock, J., & Ma, R. 2015, ApJS, 217, 21
Fang, T., Mckee, C. F., Canizares, C. R., & Wolfire, M. 2006, ApJ, 644, 174
Freire, P. C., Kramer, M., Lyne, A. G., et al. 2001, ApJL, 557, L105
Gaensler, B. M., Madsen, G. J., Chatterjee, S., & Mao, S. A. 2008, PASA, 25, 184
Good, D. C., Andersen, B. C., Chawla, P., et al. 2021, ApJ, 922, 43
Graczyk, D., Pietrzyński, G., Thompson, I. B., et al. 2020, ApJ, 904, 13
Grcevich, J., & Putman, M. E. 2009, ApJ, 696, 385
Gupta, A., Galeazzi, M., Koutroumpa, D., Smith, R., & Lallement, R. 2009, ApJ, 707, 644
Gupta, A., Mathur, S., Krongold, Y., Nicastro, F., & Galeazzi, M. 2012, ApJL, 756, L8
HI4PI Collaboration, Ben Bekhti, N., Flöer, L., et al. 2016, A&A, 594, A116

Hall, P., Park, B. U., & Stern, S. E. 1998, J. Multivar. Anal., 66, 71
Heintz, K. E., Prochaska, J. X., Simha, S., et al. 2020, ApJ, 903, 152
Henley, D. B., & Shelton, R. L. 2013, ApJ, 773, 92
Henley, D. B., Shelton, R. L., Kwak, K., Joung, M. R., & Mac Low, M.-M. 2010, ApJ, 723, 935
James, C. W., Prochaska, J. X., Macquart, J. P., et al. 2022, MNRAS, 509, 4775
Kaaret, P., Koutroumpa, D., Kuntz, K. D., et al. 2020, NatAs, 4, 1072
Keating, L. C., & Pen, U.-L. 2020, MNRAS, 496, L106
Kirsten, F., Marcote, B., Nimmo, K., et al. 2022, Natur, 602, 585
Kulkarni, S. R. 2020, arXiv:2007.02886
Lanman, A. E., Andersen, B. C., Chawla, P., et al. 2022, ApJ, 927, 59
Li, D., Wang, P., Zhu, W. W., et al. 2021, Natur, 598, 267
Lorimer, D. R., Bailes, M., McLaughlin, M. A., Narkevic, D. J., & Crawford, F. 2007, Sci, 318, 777
Macquart, J. P., Prochaska, J. X., McQuinn, M., et al. 2020, Natur, 581, 391
Maller, A. H., & Bullock, J. S. 2004, MNRAS, 355, 694
Manchester, R. N., Fan, G., Lyne, A. G., Kaspi, V. M., & Crawford, F. 2006, ApJ, 649, 235
Manchester, R. N., Hobbs, G. B., Teoh, A., & Hobbs, M. 2005, AJ, 129, 1993
Mathews, W. G., & Prochaska, J. X. 2017, ApJL, 846, L24
Merryfield, M., Tendulkar, S. P., Shin, K., et al. 2022, AJ, submitted (arXiv:2206.14079)
Miller, M. J., & Bregman, J. N. 2013, ApJ, 770, 118
Moretti, A., Campana, S., Lazzati, D., & Tagliaferri, G. 2003, ApJ, 588, 696
Nakashima, S., Inoue, Y., Yamasaki, N., et al. 2018, ApJ, 862, 34
Navarro, J. F., Frenk, C. S., & White, S. D. M. 1996, ApJ, 462, 563
Niu, C. H., Aggarwal, K., Li, D., et al. 2022, Natur, 606, 873
Nuza, S. E., Parisi, F., Scannapieco, C., et al. 2014, MNRAS, 441, 2593
Ocker, S. K., Cordes, J. M., & Chatterjee, S. 2020, ApJ, 897, 124
Ocker, S. K., Cordes, J. M., Chatterjee, S., et al. 2022, ApJ, 931, 87
Paladini, R., Burigana, C., Davies, R. D., et al. 2003, A&A, 397, 213
Pen, U.-L. 1999, ApJL, 510, L1
Pietrzyński, G., Graczyk, D., Gallenne, A., et al. 2019, Natur, 567, 200
Platts, E., Prochaska, J. X., & Law, C. J. 2020, ApJL, 895, L49
Planck Collaboration, Adam, R., Ade, P. A. R., et al. 2016a, A&A, 594, A10
Planck Collaboration, Ade, P. A. R., Aghanim, N., et al. 2016b, A&A, 594, A13
Price, D. C., Flynn, C., & Deller, A. 2021, PASA, 38, e038
Prochaska, J. X., Macquart, J.-P., McQuinn, M., et al. 2019, Sci, 366, 231
Prochaska, J. X., & Zheng, Y. 2019, MNRAS, 485, 648
Putman, M. E., Peek, J. E. G., & Joung, M. R. 2012, ARA&A, 50, 491
Ravi, V., Catha, M., Chen, G., et al. 2023, arXiv:2301.01000
Reynolds, R. J. 1991, in IAU Symp. 144, The Interstellar Disk-Halo Connection in Galaxies, ed. H. Bloemen (Dordrecht: Kluwer), 67
Richter, P., Nuza, S. E., Fox, A. J., et al. 2017, A&A, 607, A48
Ridley, J. P., Crawford, F., Lorimer, D. R., et al. 2013, MNRAS, 433, 138
Sakai, K., Mitsuda, K., Yamasaki, N. Y., et al. 2012, in AIP Conf. Proc. 1427, Suzaku 2011: Exploring the X-ray Universe: Suzaku and Beyond, ed. R. Petre, K. Mitsuda, & L. Angelini (Melville, NY: AIP), 342
Savage, B. D., & Wakker, B. P. 2009, ApJ, 702, 1472
Schnitzeler, D. H. F. M. 2012, MNRAS, 427, 664
Sembach, K. R., Wakker, B. P., Savage, B. D., et al. 2003, ApJS, 146, 165
Shen, J., Eadie, G. M., Murray, N., et al. 2022, ApJ, 925, 1
Stanimirović, S., Putman, M., Heiles, C., et al. 2006, ApJ, 653, 1210
Tendulkar, S. P., Bassa, C. G., Cordes, J. M., et al. 2017, ApJL, 834, L7
Ueda, M., Sugiyama, H., Kobayashi, S. B., et al. 2022, PASJ, 74, 1396
Voit, G. M. 2019, ApJ, 880, 139
Wu, X., & McQuinn, M. 2022, ApJ, submitted (arXiv:2209.04455)
Yamasaki, S., & Totani, T. 2020, ApJ, 888, 105
Yao, J. M., Manchester, R. N., & Wang, N. 2017, ApJ, 835, 29
Yao, Y., & Wang, Q. D. 2007, ApJ, 658, 1088
Yoshino, T., Mitsuda, K., Yamasaki, N. Y., et al. 2009, PASJ, 61, 805